Insight on Shallow Trap States in Boosting Electrochemiluminescence Efficiency of Carbon Nitrides

Yanfeng Fang,‡ Hong Yang,‡ Yuhua Hou, Yanfei Shen*, Songqin Liu, Yuanjian Zhang*

Jiangsu Engineering Laboratory of Smart Carbon-Rich Materials and Device, Jiangsu Province Hi-Tech Key Laboratory for Bio-Medical Research, State Key Laboratory of Bioelectronics, School of Chemistry and Chemical Engineering, Medical School, Southeast University, Nanjing 211189, China.

E-mail: Yanfei.Shen@seu.edu.cn (Y.S.), Yuanjian.Zhang@seu.edu.cn (Y.Z.)

Abstract

Highly efficient interconversion of different types of energy plays a crucial role in both science and technology. Among them, electrochemiluminescence (ECL), an emission of light excited by electrochemical reactions, has drawn attention as a powerful tool for bioassays of clinical biomarkers. Nonetheless, the quantitative description of the charge transfer kinetics within the emitter, crucial for understanding and enhancing ECL efficiency, remains elusive (Φ_{ECL}). Here, we investigated the intercalation of CN using Au nanoparticles and single atom (Au_x-CN), and the boosted charge carrier dynamics kinetics during ECL over time scales ranging from femtoseconds to seconds. Operando electrochemical impedance spectroscopy, fs-transient absorption spectroscopy, transit open circuit photovoltage and density functional theory calculations jointly disclosed Au-N bonds endowed shallow trapped electron states, which reconciled the timescale of the fast electron transfer in the bulk emitter and slow reduction of $S_2O_8^{2-}$. It ultimately accelerated the recombination rate for electron-hole pairs and further promoted the ECL performance of Au_x-CN photoelectrode. As a result, Au_x-CN showed a four-fold enhancement of Φ_{ECL} compared to the pristine CN, setting a new cathodic Φ_{ECL} record among metal-free ECL emitters and endowing a visual ECL sensor for nitrite ion, a typical environmental contaminant, with superior detection range and limit.

Introduction

Over billions of years, organisms have evolved to become incredibly efficient in energy conversion. This efficiency is essential for life, as it allows organisms to grow, reproduce, and survive. For the same reason, highly efficient interconversion of different types of energy plays a crucial role in both science and technology. Among them, electrochemiluminescence (ECL) is a type of light emission produced by electron transfer reactions between reactive species and radicals in the vicinity of electrodes in solution[1-5]. It has been successfully commercialized in bioassays for more than 150 clinical biomarkers[6-10]. In general, ECL emitters of high efficiency (Φ_{ECL}) play a central role in developing biosensors with superior sensitivity. Nonetheless, due to the intricate kinetic limitations, Φ_{ECL} of most ECL emitters in aqueous solutions is still essentially low.

To address this challenge, various innovative strategies have been proposed to enhance Φ_{ECL}. For instance, accelerating electron transfer at interfaces among electrodes, emitters and co-reactants using shortened distances[11-12], Schottky junctions[13] or catalytic effects[14] leads to a significantly improved Φ_{ECL} for a variety of emitters. Suppression of non-radiative relaxation[12, 15-20] (e.g., by aggregation/crystallization, host-guest recognition, and ligand-induced assembly), and pre-oxidation/reduction of emitters[21-22] provide alternative routes to booster Φ_{ECL}. In principle, the physical and chemical properties of materials are intrinsically bestowed by interactions over not only different length scales but also variable timescales. Typical ECL with co-reagents, contains mixed multiple charge-transfer pathways, including electron transfer in bulk emitters, redox reactions at emitters/co-reagents interface, and electron transition between excited and ground states. Notably, however there are huge timescale mismatches among them from nanoseconds to milliseconds. From an overall perspective, although challenging, unambiguously revealing ECL kinetics of each process is decisive in extracting the rate-determining step and therefore making a timescale reconcilement of them would open a new methodology to further boost Φ_{ECL}. Nonetheless, to the best of our knowledge, a complete quantitative description and coordination of ECL kinetics for diverse charge transfer processes at different timescales have still been lacking.

Herein, we report the timescale coordination of ECL kinetics for carbon nitrides (CN) by Au-N bond functionalization. Different to the conventional physical absorption of Au at surfaces or intercalation in layers, the Au-N bonds were established between adjacent CN layers. Quantitative kinetic studies revealed the Au-N bonding not only promoted the electron transfer in the bulk CN but also endowed a new shallow trapped electron state. Due to the electron sink effect, the timescale mismatch between the slow redox reaction at diffusion layers and fast electron transfer in bulk CN was reduced. Moreover, the emissive shallow trapped electrons exhibited a faster electron transition kinetics between excited and ground states. As a result, Au_x-CN showed a four-fold enhancement of Φ_{ECL} compared to the pristine CN, setting a new cathodic Φ_{ECL} record among metal-free ECL emitters. This work provides a new approach to boost Φ_{ECL} by timescale coordination of each kinetic step in ECL.

Results and discussion

Synthesis and structural characterization of Au_x-CN photoelectrode. As a metal-free polymeric semiconductor, 2D carbon nitride (CN) has drawn increasing attention as a new generation of conjugated polymer-based ECL luminophore[23-26]. It demonstrates intriguing properties, such as abundant availability, high stability, excellent biocompatibility, and record-level cathodic Φ_{ECL} among metal-free ECL emitters[27-28]. To modulate the timescales of each ECL process of CN, herein we report the doping of CN via Au-N bond functionalization (Au_x-CN). The general procedures for CN and Au_x-CN photoelectrode preparation were shown in **Figure 1a**. Briefly, a clean fluorine doped tin oxide (FTO) glass was immersed into a hot (80 °C) saturated cyanamide solution with or without $HAuCl_4$. A uniform crystal film was firmly coated on FTO after cooling. The final CN and Au_x-CN photoelectrodes were prepared by calcination of the crystal films at 500 °C for 4 h under N_2 atmosphere. The scanning electron microscopy (SEM) of CN and Au_x-CN photoelectrodes exhibited a continuous film on FTO with an intimate interface (**Figure S1**). Scratch-track morphologies showed no obvious cracks, indicating the good toughness of the CN and Au_x-CN photoelectrodes (**Figure S2**). To disclose the Au species in the

interlayer of CN, the scanning transmission electron microscopy (STEM) images were measured. As shown in **Figures 1b and c**, abundant bright spots were observed, corroborating the co-existence of uniformly dispersed Au nanoparticles (NPs) and single atoms (SA) in the adjacent layer of the CN matrix. High-resolution TEM (HRTEM) of Au_x-CN showed a typical Au (111) plane with a characteristic lattice spacing of 0.235 nm was observed (**Figure 1b** inset)[24, 29]. The corresponding high-resolution STEM-energy dispersive spectrometer (EDS) elemental mapping images showed that the C, N, and Au were homogeneously dispersed across the entire CN (**Figure S3**). The inductively coupled plasma-optical emission spectroscopy (ICP-OES) analysis showed that the Au loading in Au_x-CN was 0.06 wt %, indicating only a minor structural disorder was introduced into the pristine CN structure.

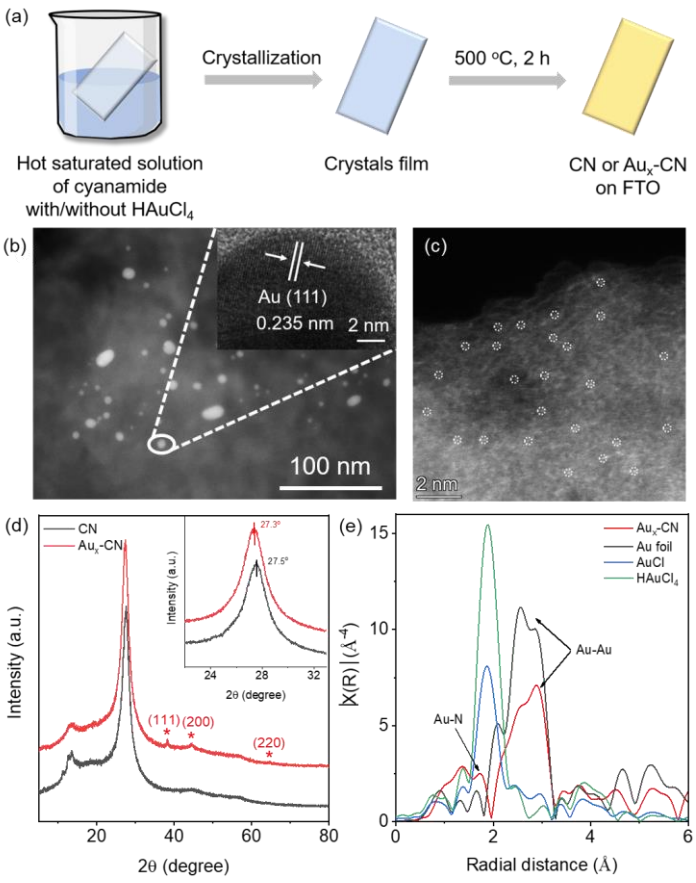

Figure 1. Synthesis and structural characterization of Au_x-CN photoelectrode. (a) Scheme of the general fabrication procedure for CN and Au_x-CN on the FTO. (b) STEM and (c) HAADF-STEM images of Au_x-CN. Inset of (b): HRTEM image of Au_x-CN. (d) XRD patterns of CN and Au_x-CN. The asterisk indicates the diffraction from Au NPs. (e) Fourier transforms of the EXAFS spectra of Au_x-CN and the reference samples.

The layered crystal structures of Au_x-CN were investigated by X-ray diffraction (XRD, **Figure 1e**). A series of characteristic diffraction peaks at 2θ=34.4°, 44.7° and 64.8° belonging to (111), (200) and (220) crystal planes of Au NPs were slightly observed for Au_x-CN, further confirming the cubic crystal structure of the intercalated Au NPs[30]. Moreover, the XRD peak of Au_x-CN at 27.3° was observed, which could be assigned to interlayer stacking (002) of the conjugated aromatic systems[31]. Compared to that of CN (27.5°), it was shifted to a smaller angle, which was consistent with TEM analysis, indicative of a thicker interlayer distance due to intercalated Au species[32]. The Fourier transform infrared (FTIR, **Figure S4**), X-ray photoelectron spectroscopy (XPS, **Figure S5**) and matrix-free laser desorption/ionization time-of-flight mass (LDI-TOF-MS, **Figure S6**) spectra verified the intercalated Au rarely damage the CN framework. The changes in the energy band structure were due to the incorporation of the Au species into CN (**Figure S7**).

To explore the chemical state of Au in Au_x-CN, the X-ray absorption near-edge structure (XANES) was conducted at the Au L3-edge. As shown in **Figure S8**, the absorption edge for Au_x-CN was located between $HAuCl_4$ and Au foil references, and closer to that of AuCl, implying that the Au species carry slightly positive charges[33-34]. The valance state of Au_x-CN was further confirmed by the X-ray photoelectron spectroscopy (XPS). The XPS spectra of Au_x-CN (**Figure S9)** showed the typical 4f5/2 and 4f7/2 signals at 89.7 and 83.4 eV, assigning to the oxidation state (Au^I) and metallic state (Au^0)[33], respectively. To disclose the coordination environment of Au species in Au_x-CN, the extended X-ray absorption fine structure (EXAFS) spectroscopy was investigated at the Au L3-edge. **Figure 1f** showed the Fourier transforms of the Au L3-edge EXAFS oscillations of the as-prepared Au_x-CN. It was obvious that the peaks at 2.0-3.3 Å were assigned to the Au-Au bond corresponding to Au NPs, while the peak located at approximately 1.7 Å could be ascribed to the scattering path of Au-N(C)[33-34]. According to this bond length, the density functional theory (DFT) calculation further verified that the Au-N bond was positioned between the interlayer of CN, rather than the cavity of the tri-s-triazine framework in the basal plane of CN. Therefore, by a simple co-polymerization method, Au-N bonding was introduced into the interlayer of CN.

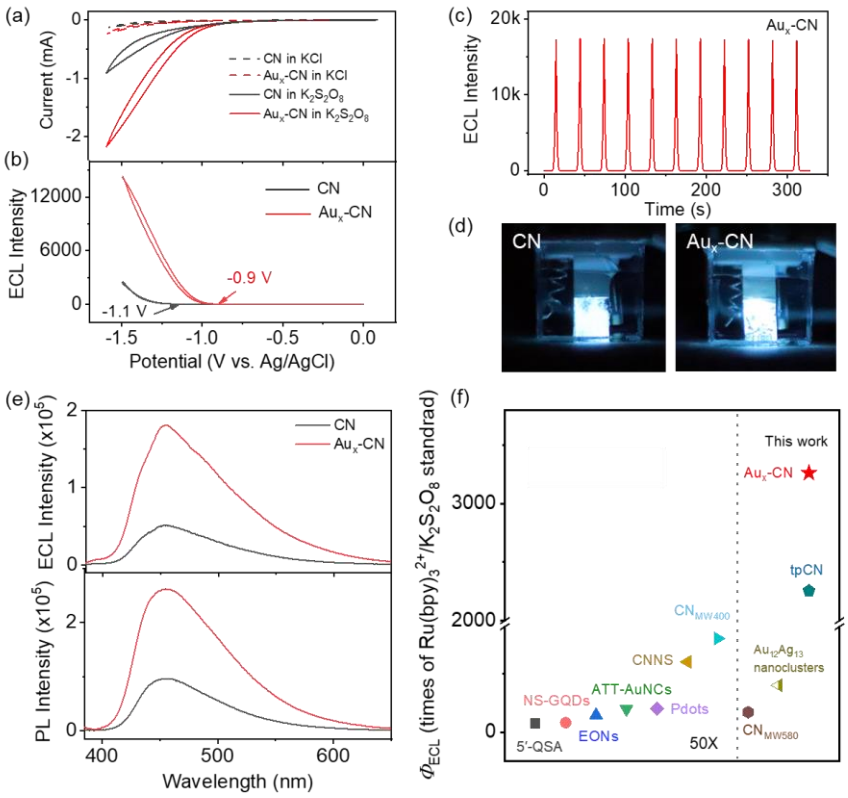

Figure 2. ECL performance of Au$_x$-CN photoelectrode. (a) CV and (b) ECL curves of CN and Au$_x$-CN photoelectrode. Electrolytes: 0.01 M PBS containing 0.1 M KCl with or without 25 mM $K_2S_2O_8$. (c) ECL response of CN and Au$_x$-CN photoelectrode under continuous CV scans. (d) Photographs of CN and Au$_x$-CN photoelectrode under -1.5 V vs. Ag/AgCl. (e) ECL and fluorescence spectrum of CN and Au$_x$-CN photoelectrode. (f) ECL efficiency comparison of Au$_x$-/CN photoelectrode and other counterparts in previous reports.

ECL performance of Au$_x$-CN photoelectrode. The cyclic voltammogram (CV) curve provided the initial energy to trigger the ECL. As shown in **Figure 2a**, a minor current in CV curves was measured in the solution without $K_2S_2O_8$ both for CN and Au$_x$-CN photoelectrode, indicating negligible polarization of water during the reduction of $K_2S_2O_8$. Notably, the reduction peak of $K_2S_2O_8$ was out of the scope of the electrochemical window. It was attributed to the high iR drop of CN and Au$_x$-CN photoelectrode[35]. **Figure 2b** showed the ECL onset potential of Au$_x$-CN photoelectrode positively shifted by 200 mV compared to that of CN photoelectrode. As shown in **Figure S10**, different Au loadings were examined to assess the ECL intensity of the Au$_x$-CN photoelectrode, and the intensity reached almost 4 times of that the CN photoelectrode. The ECL of Au$_x$-CN photoelectrode

was stable under continuous CV scans (**Figure 2c**) and the intense emission can be easily observed by the naked eye (**Figure 2d**). **Figure 2e** showed the ECL peak centered at ca. 455 nm, almost identical to the fluorescence spectrum, manifesting the CB-VB transition mechanism, different from many nanostructured ECL emitters with defective state emission[28]. An easily reproducible $Ru(bpy)_3^{2+}/K_2S_2O_8$ aqueous system was used as a reference to facilely compare Φ_{ECL} with different luminophores in this study (see the detailed discussion of the justification and calculation methods in the Experimental section of SI and **Figures S11** and **12**). As shown in **Figure 2f**, the Au_x-CN photoelectrode reached 3261 times the aqueous $Ru(bpy)_3^{2+}/K_2S_2O_8$ reference, which set a new record of Φ_{ECL} for CN family and were higher than those of most reported luminophores, to the best of our knowledge (**Table S1**).

Electron transfer processes of ECL in Au_x-CN. The co-reactant typed ECL (e.g., $Ru(bpy)_3^{2+}$) has been elucidated in detail for four possible reaction routes (**Figure S13**)[36]. Three of them are involved in the direct oxidation of co-reactants on the electrode surface (**Figure S13a-c**). Especially, for the CN and Au_x-CN photoelectrode, the redox reaction was evidently inhibited by ca. 1000 times compared with bare FTO in regard to the interfacial charge transfer resistance across the electrode/electrolyte (R_{ct}, **Figure S14** and **Table S2**). It suggested that the co-reactants accepted electrons from CN or Au_x-CN, rather than the conventional substrate electrode. The general ECL mechanisms of Au_x-CN/$K_2S_2O_8$ system are shown in **Eq. 1-4**[28]. Briefly, electrons were injected from FTO substrate electrodes into the conduction band (CB) of CN to form Au_x-$CN^{\bullet-}$ (**Eq. 1**). Next, a few excited electrons obtained from Au_x-$CN^{\bullet-}$ reduced co-reagents, producing strong oxidant $SO_4^{\bullet-}$ (**Eq. 2**), which subsequently generated holes in the valence band (VB, **Eq. 3**) by an additional one-electron extraction. Lastly, the electrons in the CB and the holes in the VB recombined with the emission of light (**Eq. 4**).

$$Au_x\text{-}CN + e^- \rightarrow Au_x\text{-}CN^{\bullet-} \quad \textbf{[Eq. 1]}$$

$$S_2O_8^{2-} + Au_x\text{-}CN^{\bullet-} \rightarrow SO_4^{2-} + SO_4^{\bullet-} + Au_x\text{-}CN \quad \textbf{[Eq. 2]}$$

$$Au_x\text{-}CN^{\bullet-} + SO_4^{\bullet-} \rightarrow Au_x\text{-}CN^{*} + SO_4^{2-} \quad \textbf{[Eq. 3]}$$

$$(SO_4^{\bullet-} \rightarrow SO_4^{2-} + h^+)$$

$$Au_x\text{-}CN^{*} \rightarrow Au_x\text{-}CN + h\nu \quad \textbf{[Eq. 4]}$$

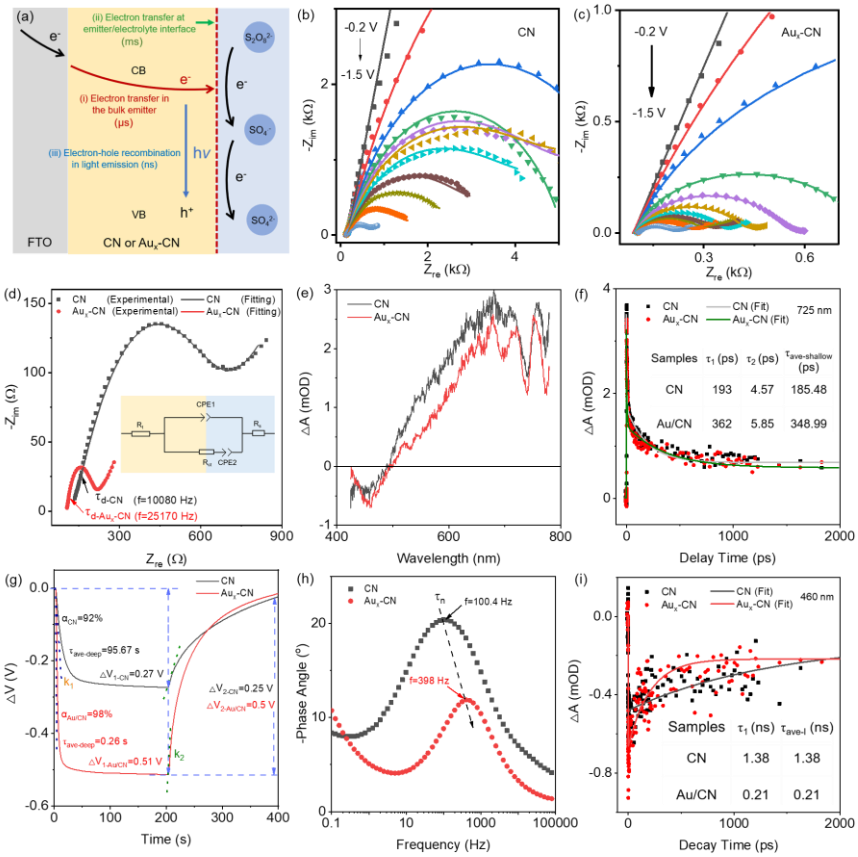

Figure 3. Electron transfer pathways and kinetics in Au$_x$-CN. (a) Possible charge transfer processes of ECL in Au$_x$-CN. Nyquist plots for (b) CN and (c) Au$_x$-CN photoelectrode at different applied potentials versus Ag/AgCl in 0.01 M PBS containing 0.1 M KCl and 25 mM $K_2S_2O_8$. Scatters and lines represent the experiment and fitted data, respectively. (d) Nyquist plots for CN and Au$_x$-CN photoelectrode at -1.5 V vs. Ag/AgCl. Inset: Simplified equivalent circuit. R_t: electron transport resistance. R_{ct}: the charge reaction resistance. Constant phase element (CPE1): non-ideal capacitance. CPE2: non-ideal Warburg element. R_s: solution resistance. (e) Femtosecond transient absorption spectra of CN and Au$_x$-CN photoelectrode at 5 fs delays under a 365 nm pump. (f) Representative ultrafast transient absorption kinetics probed at 725 nm (pump at 365 nm) for CN and Au$_x$-CN photoelectrode. (g) Open circuit potential of CN and Au$_x$-CN photoelectrode under chopped visible light irradiation in 0.1 M KCl. (h) Bode plots for CN and Au$_x$-CN photoelectrode at -1.5 V vs. Ag/AgCl. (i) Representative ultrafast transient absorption kinetics probed at 460 nm (pump at 365 nm) for CN and Au$_x$-CN photoelectrode.

(1) Electron transfer kinetics in bulk ECL emitters. To verify electron transfer in the bulk ECL emitter (**Eq. 1)**, the operand electrochemical impedance spectroscopy (EIS) under different potentials, the fs-transient absorption spectra (fs-TAS), and the open circuit photovoltage were explored. Before that, the photothermal effect and the plasma resonance

effect were excluded by control experiments, as negligible temperature variations (**Figure S15)** and plasma resonance effects of Au species (**Figure S7b**) were observed for the CN and Au_x-CN photoelectrodes. As shown in **Figures 3b** and **3c**, at the low voltage, Nyquist plots revealed approximated straight lines, which indicated high charge reaction resistance. When the voltage increased, a more complete semicircle appeared in the Nyquist plots, suggesting the Faradaic reaction occurred[37-38]. Moreover, the CN and Au_x-CN photoelectrode started to exhibit Warburg impedance at -1.5 V and -1.0 V, respectively. The lower voltage value indicated that the CN photoelectrode had a limit in charge transfer resistance, presumably due to its poor electronic conductivity[37-38]. As shown in **Figure 3d**, the Nyquist plots showed straight lines in the high-frequency part at -1.5 V. This type of EIS pattern belonged to the transmission line model **(Figure S17)**[39-40], and the simplified equivalent circuit models were shown in **Figure 3d** inset (see the fit parameters in **Tables S3** and **S4)**. As summarized in **Figure S18**, the values of electron transport resistance (R_t) remained almost constant under different applied voltages, indicating R_t was an intrinsic property of emitters. The R_t values for CN photoelectrode were approximately 5 times higher than that of Au_x-CN photoelectrode, suggesting the improved electron conductivity of Au_x-CN photoelectrode[38].

To confirm the carrier diffusion dynamics in bulk emitters, the carrier diffusion time (τ_d) and electron mobility (μ) of CN and Au_x-CN photoelectrode at ECL work conditions were also analyzed from the EIS spectra. As shown in **Figure 3d**, the inflection point between the straight line and arc in the high-frequency part was associated with τ_d, which was inversely correlated with the frequency[41-42]. The τ_d of CN and Au_x-CN photoelectrode were calculated to be 99 and 39 μs, respectively. And the electron mobility was calculated using the Nernst-Einstein equation[42-43]:

$$\mu = \frac{eL^2}{k_B T \tau_d} \qquad \textbf{[Eq. 5]}$$

where e is the electronic charge, L is the effective travel distance of carriers through the active layer (3 μm in this work), k_B is the Boltzmann constant, and T is the absolute temperature. The electron mobility of the Au_x-CN photoelectrode was calculated as 8.98 x 10^{-2} cm^2 V^{-1} s^{-1}, which was 3 times higher than that of the CN photoelectrode (3.54 x 10^{-2}

$cm^2\ V^{-1}\ s^{-1}$). The significantly reduced τ_d and improved electron mobility of the Au_x-CN photoelectrode indicated the faster carrier diffusion kinetics in the bulk Au_x-CN photoelectrode. Therefore, in the bulk CN, electron diffusion kinetics was boosted after the introduction of the Au-N bond in the interlayer of CN.

To investigate the electron states in bulk emitters, the fs-TAS was conducted. **Figure 3e** exhibited a positive absorption from 500 to 780 nm and a negative absorption from 425 to 500 nm in the fs-TAS of CN and Au_x-CN photoelectrode at 5 fs delays under a 365 nm pump. The positive absorption features between 500 and 780 nm, which was highly related to photogenerated electrons in the CN[44-45]. The photoinduced absorption signal in the visible regions was partially quenched for Au_x-CN, indicative of an effective electron transfer between CN and Au species by Au-N bond[45]. To completely avoid the effects of excitation and emission, the kinetic courses of transient signals at 725 nm were used to study the electron transfer kinetics of CN and Au_x-CN photoelectrode. The fitting results showed that the electron transfer lifetime ($\tau_{ave\text{-}shallow}$) of CN and Au_x-CN photoelectrode were 185.48 and 348.99 ps, respectively (**Figure 3f**). The increased lifetime suggested that the near band-edge shallow electron trap states of CN, most presumably introduced/strengthened by Au-N bonding, offered more opportunities for excited electrons to participate ECL[46].

The OCP under chopped light was further measured to study the deep trapped long-lived electrons state (**Figure 3g**). The surface deep electron trap state could be evaluated by the ratio of photovoltage value (α) after light on (ΔV_1) and off (ΔV_2). It is commonly believed that low α is related to the electron deep trap state[35]. It was observed that the value of α was closer to 1 for Au_x-CN photoelectrode, suggesting a less surface deep electron trap state. The electron lifetimes were calculated by fitting the photovoltage decay curves[47-48]. As shown in **Figure S19**, the average charge lifetime ($\tau_{ave\text{-}deep}$) for CN photoelectrode was 149.04 s, which was 2 times of magnitude longer than Au_x-CN photoelectrode (61.76 s). In general, the long average lifetime indicated a severe electron trap effect[48]. Thus, the OCP measurement disclosed that Au_x-CN photoelectrode had less surface deep trapping state of electrons, which would lead to a higher efficiency of electron utilization in ECL.

Moreover, the OCP measurement disclosed that Au_x-CN photoelectrode had higher excited electron-storage capacity, which was favorable for excitation and faster electron-hole recombination kinetics (see more detailed discussion in **Figure S20**).

(2) Electron transfer kinetics at emitter/co-reagent interface. We next explored the co-reagent reduction at the Au_x-CN/$S_2O_8^{2-}$ interface (**Eq. 2 and 3)**. The phase angle vs. frequency plots at different potentials (**Figure S21**) of CN and Au_x-CN photoelectrode were used to probe the electron reaction kinetic at the emitter/$S_2O_8^{2-}$ interface during the ECL process. The peak at the mediate frequency region is related to the effective lifetime[41-42] (τ_n, **Figure 3h**). The τ_n of CN and Au_x-CN photoelectrode from EIS bode plots was approximately 4 times smaller than that of CN photoelectrode at different overpotentials (**Figure S22**) and the values of τ_n for CN and Au_x-CN photoelectrode was 9.9 ms and 2.5 ms at work conditions. In general, a shorter lifetime was associated with the faster electron transfer kinetic at the emitter/$S_2O_8^{2-}$ interface. As shown in **Figure S23**, the R_{ct} for Au_x-CN photoelectrode obtained from EIS fitting was approximately 10 times smaller than that of CN photoelectrode at different overpotentials, indicating the reduction of $S_2O_8^{2-}$ was more ready to occur at the Au_x-CN/$S_2O_8^{2-}$ interface. Therefore, in the bulk CN, electron transfer kinetics at the emitter/co-reagent interface was boosted after the introduction of a more efficient shallow electron trapping state.

(3) Electron-hole recombination kinetics in light emission. To understand the influencing factors for the emissive state in ECL (**Eq. 4**), the fs-TAS, electron-hole recombination efficiency (η_{re}) and time-resolved FL spectra were measured. **Figure 3e** exhibited a negative absorption from 425 to 500 nm in the fs-TAS of CN and Au_x-CN photoelectrode, which was associated with the stimulated emission[45, 47]. The lower TAS intensity indicated increased electron-hole recombination for Au_x-CN photoelectrode, which was consistent with the higher FL intensity in **Figure 2e**. Accordingly, as shown in **Figure S24**, the calculated η_{re} (**Eq. 6**) of CN and Au_x-CN photoelectrode was calculated to be 47% and 65.6%. Moreover, the TA signal of Au_x-CN photoelectrode decreased to almost zero within 1 ns after photoexcitation, while that of CN did not, suggesting a fast electron-hole recombination (**Figure S25**)[47]. The fitting result of the negative signal was

demonstrated in **Figure 3i**. The electron-hole recombination lifetime (τ_l) of Au_x-CN photoelectrode fitted at 460 nm was 0.21 ns and this value was nearly 7 times shorter than that of CN photoelectrode (1.38 ns). Moreover, the FL decay lifetime for CN and Au_x-CN photoelectrode was also measured to be 3.46 ns and 1.69 ns, respectively (**Figure S26**). In general, a shorter TAS and FL decay lifetime of the radiative process often indicates a faster recombination rate for electron-hole pairs[35]. In this sense, the enhanced electron-hole recombination efficiency and decreased lifetime were observed, indicative of the critical role of the Au-N bond, most presumably via a more efficient shallow electron trap state.

$$\eta_{re}(\%) = 1 - \frac{J_{KCl}}{J_{TEOA}} \times 100\% \qquad \textbf{[Eq. 6]}$$

J_{KCl} is the photocurrent density obtained in 0.1 M KCl aqueous solution, while J_{TEOA} is the photocurrent density obtained in 0.1 M KCl containing 10% (v/v) triethanolamine (TEOA).

Table 1. Quantitative kinetic parameters of electron transfer for the ECL of CN and Au_x-CN.

Electron transfer stage	Parameters	CN	Au_x-CN
In bulk ECL emitter	τ_d (μs)	99	39
	μ ($cm^2\ V^{-1}\ s^{-1}$)	3.54 x 10^{-2}	8.98 x 10^{-2}
	$\tau_{avg\text{-}shallow}$ (ps)	185.48	348.99
	$\tau_{ave\text{-}deep}$ (s)	149.04	61.76
At the emitter/co-reactant interface	τ_n (ms)	9.9	2.5
During light emission	$\tau_{avg\text{-}l}$ (ns)	1.38	0.21
	η_{re} (%)	47%	65.6%

$\tau_{ave\text{-}shallow}$: shallow electron trap state lifetime; τ_d: carrier diffusion lifetime; $\tau_{ave\text{-}deep}$: deep electron trap state lifetime; μ: electron mobility; τ_n: electron transfer lifetime; $\tau_{ave\text{-}l}$: electron-hole recombination lifetime obtained from TAS; η_{re}: electron-hole recombination efficiency.

Given the above, the quantitative values of kinetic parameters for electron transfer in the ECL of CN and Au_x-CN were shown in **Table 1**. The roles of Au in the electron transfer in the ECL of Au_x-CN were summarized as follows. The formation of Au-N bonds accelerated the electron transfer in the bulk Au_x-CN photoelectrode. More importantly, it endowed a new shallow trapped electron state that had a longer lifetime, thus smoothing out the timescale inconsistencies of electron transfer at different stages. The shallow-trapped electrons in the bulk emitter that existed at about the picosecond time scale extended 2 times magnitude by the Au-N bond functionalization, which coordinated the slow charge transfer at the emitter/co-reactant interface in the microsecond time scale. It would increase the reduction of co-reactants at the interface, and further improve the electron-hole recombination rate and efficiency for the ECL of Au_x-CN. In contrast, the accumulation of long-lived, deeply trapped electrons, detrimental to efficient ECL, was effectively suppressed. It should be noted that while the intricate interplay of charge transfer kinetics in ECL has rarely been quantitatively dissected, the profound influence of charge carrier traps on ECL performance, despite their extensive exploration in organic semiconductors for diverse time scales, remains largely elusive. Harnessing quantitative kinetic study tools like operando EIS, transit OCP, and TAS, this study unveils how incorporating appropriate trap states can manipulate the timescales of substantial fluctuations in electron transfer within bulk ECL emitters, redox reactions at diffusion layers, and electron transitions between excited and ground states, thereby paving the way to enhance ECL efficiency.

Molecular insights of ECL enhancement by DFT calculations. The influence of Au-N bonds on accelerating the electron transfer and generating a new shallow electron trapping state in the Au_x-CN photoelectrode was explored by the DFT calculation. In a simplified Au_x-CN model (see **Figure S27-S32**, see more discussion in SI), the Au-N bonds, i.e., the distance between the Au atoms and the two adjacent CN layers, were 2.06 Å and 2.07 Å, respectively, matching well with the EXAFS results (**Figure 1e**). The density of states (DOS) and the visible crystal orbitals of pristine CN and Au_x-CN were analyzed (**Figure 4**). The VBM of pristine CN (**Figures 4a** and **4c**) mainly originated from the N 2p

orbitals; whereas the CBM was contributed both by the C and N 2p orbitals. A similar electronic structure of CBM was found in Au_x-CN (**Figures 4b** and **4d**), and the contribution from Au 5d and 6s orbitals was negligible; while the VBM was mostly formed by Au 5d and 6s orbitals and N 2p orbitals. As a result, the higher-energy Au 5d and 6s orbitals recombined with the pristine CN π bonding orbitals and π anti-bonding orbitals, which made the continuity of the energy band near the CBM and VBM in Au_x-CN be improved. Consequently, charge carriers could more readily transfer in the VBM and CBM, facilitating intralayer charge transfer.

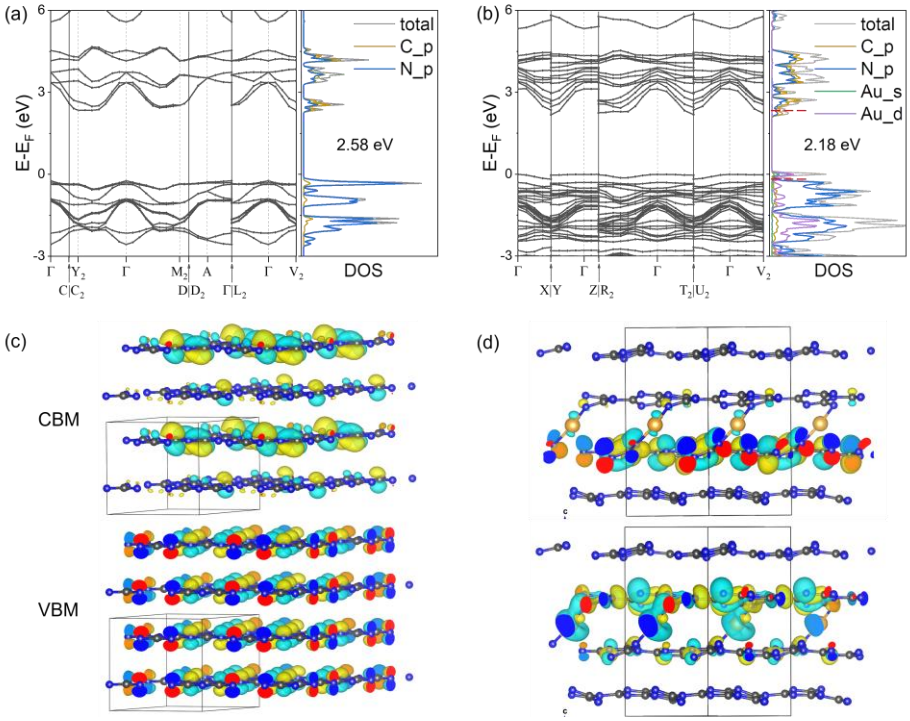

Figure 4. Band structure, DOS and VBM/CBM crystal orbitals of CN and Au_x-CN. Band structure and DOS of (a) CN and (b) Au_x-CN. Red dash lines in Au_x-CN mark the positions of CMB and VBM for CN. VBM/CBM crystal orbitals of (c) CN and (d) Au_x-CN. Gray coloring indicates carbon atoms, blue indicates nitrogen, and orange indicates gold.

In addition, inter-layer charge transfer was further analyzed by the Bader charge. The Bader charge difference between each adjacent layer of pristine CN was marginal (**Figure S33b**, $|\Delta q|$ roughly 0.0009 e^-), indicative of a very weak inter-layers charge transfer. In contrast, more electrons accumulated between each layer of Au_x-CN (**Figure S33d**, approximately 0.2 e^- of layer charge), and Au species lost 0.48 e^-. As a result, Au_x-CN

exhibited a much higher interlay charge difference (**Figure S33d**, $|\Delta q|$ roughly 0.142 e^- and 0.203 e^-), indicating Au-N_x in the CN inter-layer served as a bridge, promoting the electron transfer between the adjacent layers. Thus, the Au-N bonding improved the overall electron transfer in Au_x-CN, compared to the pristine CN.

Considering that the Au content was only 0.06 wt% in the as-prepared Au_x-CN, the band structure in Au_x-CN should still be dominated by the pristine CN. Accordingly, the band gap of Au_x-CN was 2.79 eV, which was only 0.03 eV lower than the pristine CN (**Figure S7**). Nonetheless, the large-nuclear-charge Au species enhanced conjugation within the CN layer and made CBM to shift down by 0.2 eV (red dash line in **Figure 4b**). This new state close to the CBM energy level position of pristine CN, was usually considered to be a shallow trapped electron state, in which captured electrons could be released back to the band under external stimuli, such as electric field, thereby reconciling the timescale difference of each step in ECL[49-51]. Therefore, the Au-N bonds not only accelerated the electron transfer in the bulk CN, but also created new shallow trap states near the CBM, two important factors in the improved ECL efficiency for CN.

Enhanced sensitivity in NO_2^- detection using Au_x-CN. Environmental pollution, especially water pollution, is one of the unpleasant global issues over the last few decades. Water pollution based on organic and inorganic species affects both human health and the living environment. Among them, nitrite ion (NO_2^-) is recognized as one of the common inorganic contaminants in drinking water, wastewater, and food[52-53]. Therefore, monitoring the NO_2^- concentration in drinking water and the living environment has become vital. In general, NO_2^- could consume the $SO_4^{\bullet-}$ around the electrode surface, resulting in the decrease of ECL intensity (**Figure 5a**)[35]. **Figures 5b** and **5c** showed that the cathodic ECL signal decreased gradually with the increase of NO_2^- concentration for both Au_x-CN and carbon nitride nanosheets (CNNS) photoelectrode. The logarithmic value of the ECL intensity at the Au_x-CN photoelectrode scaled linearly with the concentration of NO_2^- from 10^{-9} to 10^{-15} M, with a very low detection limit of 0.21 fM. The excellent performance of the NO_2^--based ECL biosensor has made it one of the most sensitive signal-amplification-free biosensors (**Table S5**). And, the slope of the calibration curve and linear range of Au_x-

CN photoelectrode exhibits more than 150-fold higher and 3 orders of magnitude than those of the control CNNS (**Figure 5c**). It suggested that the emitters with higher Φ_{ECL} held great potential in developing chemical sensors with superior sensitivity. Moreover, because of the exceptionally high cathodic ECL efficiency, it could be further developed into a visual cathodic ECL biosensor by the naked eye with uncompromising performance (**Figure 5e**).

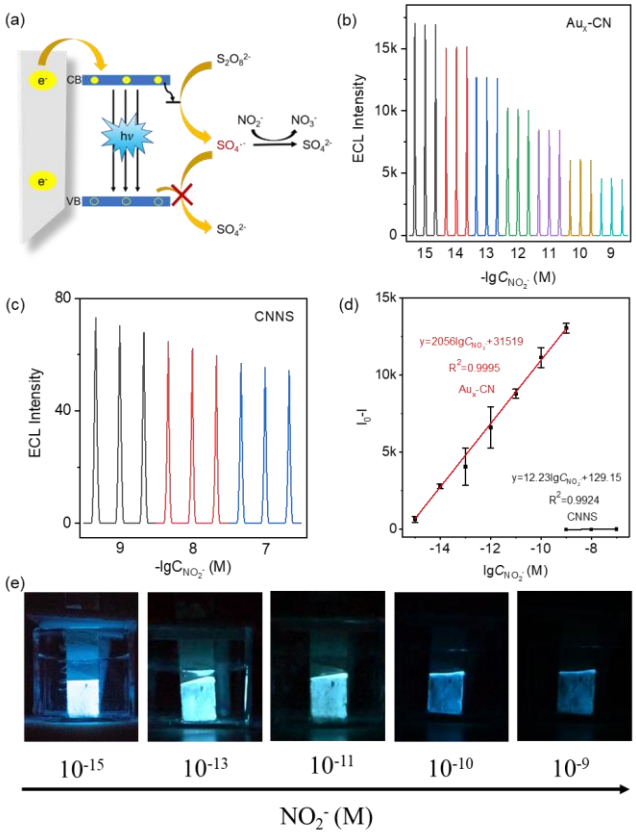

Figure 5. (a) ECL quenching mechanism upon NO_2^-. ECL curves in the presence of different concentrations of NO_2^- at (b) Au_x-CN and (c) CNNS photoelectrode. (d) Calibration curve of NO_2^- detection using Au_x-CN and CNNS photoelectrode. I_0 and I are the ECL intensity before and after addition of NO_2^-, respectively. (e) Photographs of ECL at Au_x-CN photoelectrode in solution containing different concentrations of NO_2^-.

Conclusion

In summary, we report that functionalization of Au-N bond between CN layers remarkably improved performance of ECL. The Au_x-CN photoelectrode demonstrated the highest cathodic ECL efficiency thus far (3261 times that of the $Ru(bpy)_3Cl_2/K_2S_2O_8$

reference) among the metal-free ECL emitters. This exceptionally high ECL performance is rationalized by the introduction of a shallow electron trap state associated with the Au-N bonds. Operando EIS studies revealed that the Au_x-CN photoelectrode developed 2 times shorter charge carrier diffusion lifetime in μs timescale as compared to the CN photoelectrode. Furthermore, TAS revealed that, as compared to the CN photoelectrode, there was a large portion of electrons in shallow electrons trap states in Au_x-CN and the lifetime of these electrons was extended by 2 times of magnitude into the ps timescale, which reconciled and accelerated the slow $S_2O_8^{2-}$ reduction in diffusion layers with the timescale of ms by 4 times. Meanwhile, the average deep electron lifetime observed for Au_x-CN photoelectrode was more than 2 times shorter than that of the CN photoelectrode in s timescale, which can be attributed to the faster electron transfer for Au_x-CN photoelectrode. As a result, it would increase the reduction process at the emitter/co-reactants interface in ms timescale, thus, the emissive electron-hole recombination rate and efficiency for Au_x-CN photoelectrode were promoted in ns timescale.

As such, operando EIS, TAS, and transit OCP collectively provided evidence that electrons in shallow trap states associated with Au-N bonds were key to the ECL characteristics of Au_x-CN photoelectrode. We ascribed the significant enhancement to a synergetic effect of the construction of Au-N bonds between CN layers, which provided the charge transfer driving forces for electron extraction to the photoelectrode/electrolyte interface. Meanwhile, the shallow trap state could act as an electron sink, which reconciled the timescale of the fast electron transfer in bulk emitter and slow reduction of $S_2O_8^2$, ultimately accelerating the recombination rate for electron-hole pairs and further promoting the ECL performance of Au_x-CN photoelectrode.

As a proof-of-concept application, Au_x-CN photoelectrode was successfully applied in a visual ECL sensor for a typical environmental contaminant, NO_2^-, with a wider detection range and lower detection limit, compared to the conventional CNNS. The complete quantitative description of ECL kinetics and harnessing shallow trap state in timescale coordination of each step would expand the applicability of ECL emitters in various fields of optoelectronics devices, clinical diagnosis and bioimaging.

Acknowledgments

We acknowledge XX Chen and xx Jia at Materials Characterization Center of ECNU Multifunctional Platform for Innovation for their assistance in TAS measurements. This work was supported by the National Natural Science Foundation of China (22174014 and 22074015).

Reference

(1) Ma, X.; Gao, W.; Du, F.; Yuan, F.; Yu, J.; Guan, Y.; Sojic, N.; Xu, G., *Acc. Chem. Res.* **2021,** *54* (14), 2936-2945.
(2) Luo, R.; Lv, H.; Liao, Q.; Wang, N.; Yang, J.; Li, Y.; Xi, K.; Wu, X.; Ju, H.; Lei, J., *Nat. Commun.* **2021,** *12* (1), 6808.
(3) Zanut, A.; Fiorani, A.; Canola, S.; Saito, T.; Ziebart, N.; Rapino, S.; Rebeccani, S.; Barbon, A.; Irie, T.; Josel, H.-P.; Negri, F.; Marcaccio, M.; Windfuhr, M.; Imai, K.; Valenti, G.; Paolucci, F., *Nat. Commun.* **2020,** *11* (1), 2668.
(4) Yang, X.; Hang, J.; Qu, W.; Wang, Y.; Wang, L.; Zhou, P.; Ding, H.; Su, B.; Lei, J.; Guo, W.; Dai, Z., *J. Am. Chem. Soc.* **2023,** *145* (29), 16026-16036.
(5) Cao, Z.; Li, C.; Shu, Y.; Zhu, M.; Su, B.; Qin, H.; Peng, X., *J. Am. Chem. Soc.* **2023**, DOI: 10.1021/jacs.3c10556.
(6) Dong, J.; Lu, Y.; Xu, Y.; Chen, F.; Yang, J.; Chen, Y.; Feng, J., *Nature* **2021,** *596* (7871), 244-249.
(7) Liu, Y.; Zhang, H.; Li, B.; Liu, J.; Jiang, D.; Liu, B.; Sojic, N., *J. Am. Chem. Soc.* **2021,** *143* (43), 17910-17914.
(8) Lee, J. I.; Choi, H.; Kong, S. H.; Park, S.; Park, D.; Kim, J. S.; Kwon, S. H.; Kim, J.; Choi, S. H.; Lee, S. G.; Kim, D. H.; Kang, M. S., *Adv. Mater.* **2021,** *33* (29), 2170222.
(9) Sun, Q.; Ning, Z.; Yang, E.; Yin, F.; Wu, G.; Zhang, Y.; Shen, Y., *Angew. Chem. Int. Ed.* **2023,** *62* (44), e202312053.
(10) Yan, Y.; Zhou, P.; Ding, L.; Hu, W.; Chen, W.; Su, B., *Angew. Chem. Int. Ed.* **2023**, e202314588.
(11) Wang, N.; Gao, H.; Li, Y.; Li, G.; Chen, W.; Jin, Z.; Lei, J.; Wei, Q.; Ju, H., *Angew. Chem. Int. Ed.* **2020,** *133* (1), 199-203.
(12) Wang, T.; Wang, D.; Padelford, J. W.; Jiang, J.; Wang, G., *J. Am. Chem. Soc.* **2016,** *138* (20), 6380-6383.
(13) Wu, Z.; Wen, J.; Qin, Y.; Ling, L.; Jiao, L.; Zhang, R.; Luo, Z.; Xi, M.; Hu, L.; Gu, W.; Zhu, C., *Angew. Chem. Int. Ed.* **2023,** *62* (33), e202308257.
(14) Gu, W.; Wang, H.; Jiao, L.; Wu, Y.; Chen, Y.; Hu, L.; Gong, J.; Du, D.; Zhu, C., *Angew. Chem. Int. Ed.* **2020,** *132* (9), 3562-3566.
(15) Peng, H.; Huang, Z.; Deng, H.; Wu, W.; Huang, K.; Li, Z.; Chen, W.; Liu, J., *Angew. Chem. Int. Ed.* **2019,** *132* (25), 10068-10071.
(16) Wong, J. M.; Zhang, R.; Xie, P.; Yang, L.; Zhang, M.; Zhou, R.; Wang, R.; Shen, Y.; Yang, B.; Wang, H. B.; Ding, Z., *Angew. Chem. Int. Ed.* **2020,** *59* (40), 17461-17466.
(17) Wei, X.; Zhu, M. J.; Cheng, Z.; Lee, M.; Yan, H.; Lu, C.; Xu, J. J., *Angew. Chem. Int. Ed.* **2019,** *58* (10), 3162-3166.

(18) Guo, J.; Feng, W.; Du, P.; Zhang, R.; Liu, J.; Liu, Y.; Wang, Z.; Lu, X., *Anal. Chem.* **2020,** *92* (21), 14838-14845.
(19) Ikeda, T.; Tahara, K.; Ishimatsu, R.; Ono, T.; Cui, L.; Maeda, M.; Ozawa, Y.; Abe, M., *Angew. Chem. Int. Ed.* **2023,** *62* (21), e202301109.
(20) Zhu, Z.; Zeng, C.; Zhao, Y.; Ma, J.; Yao, X.; Huo, S.; Feng, Y.; Wang, M.; Lu, X., *Angew. Chem. Int. Ed.* **2023,** *62* (46), e202312692.
(21) Jin, Z.; Zhu, X.; Wang, N.; Li, Y.; Ju, H.; Lei, J., *Angew. Chem. Int. Ed.* **2020,** *132* (26), 10532-10536.
(22) Peng, H.; Huang, Z.; Sheng, Y.; Zhang, X.; Deng, H.; Chen, W.; Liu, J., *Angew. Chem. Int. Ed.* **2019,** *131* (34), 11817-11820.
(23) Fang, Y.; Zhou, Z.; Hou, Y.; Wang, C.; Cao, X.; Liu, S.; Shen, Y.; Zhang, Y., *Anal. Chem.* **2023,** *95* (16), 6620-6628.
(24) Wu, Z.; Wen, J.; Qin, Y.; Ling, L.; Jiao, L.; Zhang, R.; Luo, Z.; Xi, M.; Hu, L.; Gu, W.; Zhu, C., *Angew. Chem. Int. Ed.* **2023,** *135* (33), e202308257.
(25) Chen, L.; Zhu, X.; Wei, J.; Tian, L.; Hu, C.; Xiang, X.; Zhou, S.-F., *Anal. Chem.* **2023,** *95* (5), 2917-2924.
(26) Zou, R.; Lin, Y.; Lu, C., *Anal. Chem.* **2021,** *93* (4), 2678-2686.
(27) Hou, Y.; Fang, Y.; Zhou, Z.; Hong, Q.; Li, W.; Yang, H.; Wu, K.; Xu, Y.; Cao, X.; Han, D.; Liu, S.; Shen, Y.; Zhang, Y., *Adv. Opt. Mater.* **2023,** *11* (6), 2202737.
(28) Zhao, T.; Zhou, Q.; Lv, Y.; Han, D.; Wu, K.; Zhao, L.; Shen, Y.; Liu, S.; Zhang, Y., *Angew. Chem. Int. Ed.* **2019,** *59* (3), 1139-1143.
(29) Wang, N.; Liu, H.; Zhou, X.; Luo, Q.; Yang, X.; Yang, H.; Shu, H.; Xu, H.; Zhang, Q.; Hildebrandt, D.; Liu, X.; Qiao, S.; Liu, B.; Feng, Q., *Adv. Funct. Mater.* **2022,** *32* (34), 2203967.
(30) Datta, K. K. R.; Reddy, B. V. S.; Ariga, K.; Vinu, A., *Angew. Chem. Int. Ed.* **2010,** *49* (34), 5961-5965.
(31) Zhou, Z.; Wang, J.; Yu, J.; Shen, Y.; Li, Y.; Liu, A.; Liu, S.; Zhang, Y., *J. Am. Chem. Soc.* **2015,** *137* (6), 2179-2182.
(32) Xiao, X.; Gao, Y.; Zhang, L.; Zhang, J.; Zhang, Q.; Li, Q.; Bao, H.; Zhou, J.; Miao, S.; Chen, N.; Wang, J.; Jiang, B.; Tian, C.; Fu, H., *Adv. Mater.* **2020,** *32* (33), 2003082.
(33) Chen, Z.; Chen, Y.; Chao, S.; Dong, X.; Chen, W.; Luo, J.; Liu, C.; Wang, D.; Chen, C.; Li, W.; Li, J.; Li, Y., *ACS Catal.* **2020,** *10* (3), 1865-1870.
(34) Chen, Z.; Zhang, Q.; Chen, W.; Dong, J.; Yao, H.; Zhang, X.; Tong, X.; Wang, D.; Peng, Q.; Chen, C.; He, W.; Li, Y., *Adv. Mater.* **2017,** *30* (5), 1704720.
(35) Fang, Y.; Hou, Y.; Yang, H.; Chen, R.; Li, W.; Ma, J.; Han, D.; Cao, X.; Liu, S.; Shen, Y.; Zhang, Y., *Adv. Opt. Mater.* **2022,** *10* (18), 2201017.
(36) Miao, W.; Choi, J.-P.; Bard, A. J., *J. Am. Chem. Soc.* **2002,** *124* (48), 14478-14485.
(37) Zhang, N.; Zou, Y.; Tao, L.; Chen, W.; Zhou, L.; Liu, Z.; Zhou, B.; Huang, G.; Lin, H.; Wang, S., *Angew. Chem. Int. Ed.* **2019,** *58* (44), 15895-15903.
(38) Xie, C.; Chen, W.; Du, S.; Yan, D.; Zhang, Y.; Chen, J.; Liu, B.; Wang, S., *Nano Energy* **2020,** *71*, 104653.
(39) Bisquert, J.; Garcia-Belmonte, G.; Fabregat-Santiago, F.; Ferriols, N. S.; Bogdanoff, P.; Pereira, E. C., *J. Phys. Chem. B* **2000,** *104* (10), 2287-2298.
(40) Mora-Seró, I.; Garcia-Belmonte, G.; Boix, P. P.; Vázquez, M. A.; Bisquert, J., *Energy*

Environ. Sci. **2009,** *2* (6), 678.
(41) Wang, Q.; Moser, J.-E.; Grätzel, M., *J. Phys. Chem. B* **2005,** *109* (31), 14945-14953.
(42) Garcia-Belmonte, G.; Munar, A.; Barea, E. M.; Bisquert, J.; Ugarte, I.; Pacios, R., *Org. Electron.* **2008,** *9* (5), 847-851.
(43) Jin, M.-J.; Jo, J.; Yoo, J.-W., *Org. Electron.* **2015,** *19*, 83-91.
(44) Godin, R.; Wang, Y.; Zwijnenburg, M. A.; Tang, J.; Durrant, J. R., *J. Am. Chem. Soc.* **2017,** *139* (14), 5216-5224.
(45) Corp, K. L.; Schlenker, C. W., *J. Am. Chem. Soc.* **2017,** *139* (23), 7904-7912.
(46) Li, X.; Bi, W.; Zhang, L.; Tao, S.; Chu, W.; Zhang, Q.; Luo, Y.; Wu, C.; Xie, Y., *Adv. Mater.* **2016,** *28* (12), 2427-2431.
(47) Ruan, Q.; Miao, T.; Wang, H.; Tang, J., *J. Am. Chem. Soc.* **2020,** *142* (6), 2795-2802.
(48) Ruan, Q.; Bayazit, M. K.; Kiran, V.; Xie, J.; Wang, Y.; Tang, J., *Chem. Commun.* **2019,** *55* (50), 7191-7194.
(49) Mandal, S.; Mukherjee, S.; De, C. K.; Roy, D.; Ghosh, S.; Mandal, P. K., *J. Phys. Chem. Lett.* **2020,** *11* (5), 1702-1707.
(50) Xue, J.; Fujitsuka, M.; Majima, T., *ACS Appl. Mater. Inter.* **2019,** *11* (43), 40860-40867.
(51) Haneef, H. F.; Zeidell, A. M.; Jurchescu, O. D., *J. Mater. Chem. C* **2020,** *8* (3), 759-787.
(52) Singh, L.; Ranjan, N., *J. Am. Chem. Soc.* **2023,** *145* (5), 2745-2749.
(53) Khachornsakkul, K.; Del-Rio-Ruiz, R.; Creasey, H.; Widmer, G.; Sonkusale, S. R., *ACS Sens.* **2023**, DOI: 10.1021/acssensors.3c01769.